

# Acoustic propagation under tidally driven, stratified flow

Steven Finette<sup>a)</sup> and Roger Oba

*Acoustics Division, Naval Research Laboratory, Washington, DC 20375*

Colin Shen and Thomas Evans

*Remote Sensing Division, Naval Research Laboratory, Washington, DC 20375*

(Received 27 August 2004; revised 20 October 2006; accepted 12 February 2007)

Amplitude and phase variability in acoustic fields are simulated within a canonical shelf-break ocean environment using sound speed distributions computed from hydrodynamics. The submesoscale description of the space and time varying environment is physically consistent with tidal forcing of stratified flows over variable bathymetry and includes the generation, evolution and propagation of internal tides and solibores. For selected time periods, two-dimensional acoustic transmission examples are presented for which signal gain degradation is computed between 200 and 500 Hz on vertical arrays positioned both on the shelf and beyond the shelf break. Decorrelation of the field is dominated by the phase contribution and occurs over 2–3 min, with significant recorrelation often noted for selected frequency subbands. Detection range is also determined in this frequency band. Azimuth-time variations in the acoustic field are illustrated for 100 Hz sources by extending the acoustic simulations to three spatial dimensions. The azimuthal and temporal structure of both the depth-averaged transmission loss and temporal correlation of the acoustic fields under different environmental conditions are considered. Depth-averaged transmission loss varies up to 4 dB, depending on a combination of source depth, location relative to the slope and tidally induced volumetric changes in the sound speed distribution.

[DOI: 10.1121/1.2713724]

PACS number(s): 43.30.Re, 43.30.Ft, 43.20.Mv [WLS]

Pages: 2575–2590

## I. INTRODUCTION

A significant issue in sonar system evaluation is the prediction of array performance in littoral regions where significant ocean variability is present. In this respect, the ability to simulate sensor array performance in controlled but realistic synthetic ocean environments can represent a significant contribution to a performance prediction scheme. Realistic simulation of acoustic propagation in littoral regions depends on knowledge of several quantities that characterize the ocean waveguide structure: a volumetric sound speed distribution, a set of bottom parameters and waveguide boundary conditions. This information is collectively referred to as an “environmental model.” As a step toward developing a predictive simulation capability, this paper describes a model of acoustic propagation in a littoral environment where submesoscale sound speed variability is computed in a physically consistent manner with respect to fluid motion over variable bathymetry. For littoral regions such as continental shelf-break areas, the sound speed distribution has significant space-time dependence and, therefore, an environmental model of such a region should incorporate this variability in a consistent manner with respect to external forcing and internal flows. Because of the quality of currently available numerical codes describing ocean acoustic propagation for a given sound speed distribution, the ability of an environmental model to faithfully represent a natural oceanographic environment determines, to a large extent, the predictive capa-

bility of an acoustic modeling effort. The emphasis here is on the numerical model and several example computations are presented. A direct comparison of numerical results with experimental data for a particular ocean environment is beyond the scope of this paper; that issue will be addressed in future work in order to assess the predictive capability of this approach.

A specific case is considered for illustrative purposes, that of an idealized continental shelf-break environment where tidally driven flow of stratified water over variable bathymetry induces volume variability in the form of internal tides and nonlinear wave packets. The latter are often referred to as solitary wave packets or solibores. These oceanographic features impact acoustic field propagation and subsequent array performance through their effect on the sound speed field. The sound speed distribution is determined here by first solving the Navier–Stokes equations of fluid dynamics which describe the space–time temperature, salinity and non-hydrostatic pressure fields, and then mapping these distributions into sound speed using a phenomenological relationship. Simulations of the influence of tidal flow on acoustic propagation are presented using this environmental model in conjunction with acoustic field calculations provided by two-dimensional (2D) and three-dimensional (3D) wide-angle parabolic equation codes.

A combined oceanographic-acoustic experiment, SWARM95,<sup>1</sup> served as a stimulus for a number of modeling efforts related to the interaction of acoustic fields with both internal tides and solitary wave packets. Although these studies used relatively simple models to describe the volume variability of the sound speed field linked to these oceanographic

<sup>a)</sup>Electronic mail: steven.finette@nrl.navy.mil

graphic features, they yielded significant insights into the nature of this interaction. The early emphasis was first placed on scintillation index<sup>2</sup> and mode coupling<sup>2-5</sup> along the direction of propagation of the wave packet using simplified packet wave-form shapes to describe the isopycnal displacements and resulting sound speed perturbations. More complex waveforms based on weakly nonlinear theories of solitary wave propagation were also considered. These included the cnoidal<sup>6</sup> and dnoidal<sup>5,7</sup> elliptic functions that more closely resembled some of the isopycnal variations found in experimental data. The relationship between the acoustic field structure and source/receiver orientation with respect to the solitary wave propagation vector was described using  $N \times 2D$  single frequency<sup>6</sup> and pulse<sup>7</sup> calculations of the acoustic field, without the inclusion of horizontal refraction. The effects of horizontal refraction on both acoustic field intensity and horizontal (cross range or transverse) coherence are inherently 3D and have been analyzed using both analytic<sup>3,8,9</sup> and numerical simulation techniques.<sup>10,11</sup> Relationships between horizontal array beamforming and horizontal refraction induced by solitary wave packets have been described recently.<sup>12</sup>

Mesoscale ocean models have been applied to describe the evolution of large-scale sound speed distributions for some time.<sup>13,14</sup> This class of ocean models filter out spatially localized internal gravity waves that are ubiquitous in continental shelf regions. As these waves have a significant effect on the amplitude and phase of an acoustic field propagating through the region, a more comprehensive hydrodynamic model of littoral oceanography is considered here by describing the environment with a submesoscale ocean model, representing recent developments in simulating ocean dynamics.<sup>15-19</sup> The submesoscale models can naturally include, in a physically consistent formalism, the generation, propagation, and dissipation of internal waves driven by tidal forcing as well as other oceanographic features such as fronts, jets and overturning bores. Recently, there have been attempts to evaluate the influence of some of these finer scale ocean structures on acoustic propagation.<sup>20-22</sup> Our view is that the extra effort involved with the design and implementation of submesoscale ocean models to estimate the sound speed field for use in acoustic propagation studies of sonar performance is mitigated by a corresponding increased flexibility in describing littoral environments, the potential enhancement to acoustic predictive schemes and future advances in computer hardware. The issue of whether these models enhance predictability over that obtainable through either mesoscale modeling or by use of approximate approaches involving, e.g., weakly nonlinear Korteweg-de Vries (KdV) descriptions of internal waves is an important issue in performance prediction but is not considered here. It can only be resolved by quantitative comparisons of simulation results with experimental data, taking into account the environmental uncertainty in the parameters, fields, and model initialization describing the simulated environment. Such model/data comparisons have a host of issues that would need to be considered, though it is worth making a brief comment here to distinguish between the verification and validation procedures needed to develop a simulation-

based prediction scheme. The results presented in this paper are based on codes that were benchmarked as part of a validation procedure to ensure that they properly represent, in a numerical form to some level of accuracy, the mathematical description of the system (ocean environment and acoustic field). Verification, on the other hand, depends on computing metrics which assess the ability of the numerical model to predict or represent experimental acoustic data. The spatial and temporal sampling requirements needed to execute a submesoscale code reflect the underlying scales of the physics to be represented and correspond to much finer sampling of the boundary/initial conditions and ocean volume than is normally available in partially controlled, at-sea experiments for which temperature and salinity are sparsely sampled. The resulting information deficit presents a significant challenge in the validation phase where the “value-added” of submesoscale modeling over other approaches for making acoustic predictions needs to be addressed.

Section II briefly describes the environmental model and implementation, whereas Sec. III demonstrates its use through examples of acoustic propagation in a canonical shelf-break environment where it is assumed that the sound speed dynamics is driven exclusively by tidal flow. Both signal gain degradation and detection range are computed under stratified flow as a function of frequency and related to the oceanographic state of the environment as a function of time. The azimuthal dependence of the acoustic field on both bathymetry and tidal flow is then discussed in the context of a simple cross-range extension of the shelf break environment in conjunction with 3D acoustic simulations. A summary and discussion are given in Sec. IV.

## II. ENVIRONMENTAL DYNAMICS

The submesoscale hydrodynamic model used in the following analysis is briefly considered in this section.<sup>17,18</sup> The ocean environment is described through the equations of motion for an incompressible fluid in the Boussinesq approximation, where the density variations are retained only in the buoyancy term.<sup>23</sup> This approximation is excellent for littoral ocean environments. The dynamics are represented by a set of coupled partial differential equations describing the Lagrangian fluid particle velocity  $\mathbf{u}(\mathbf{r}, t)$ , pressure  $p(\mathbf{r}, t)$ , density  $\rho(\mathbf{r}, t)$ , temperature  $T(\mathbf{r}, t)$ , and salinity  $S(\mathbf{r}, t)$  fields, where  $\mathbf{r}=(x, y, z)$ , and  $\mathbf{u}=(u, v, w)$  specify the three Cartesian velocity components ( $dx/dt, dy/dt, dz/dt$ ). Water depth is associated with the  $z$  direction, negative toward increasing water depth. Here, the ocean surface is free to move under external tidal forcing, a feature often suppressed in ocean modeling. The momentum equation is expressed as

$$\frac{D\mathbf{u}}{Dt} + \mathbf{f} \times \mathbf{u} = -\frac{\nabla p}{\rho_o} + \mathbf{g} \frac{\rho}{\rho_o} + \mu \nabla^2 \mathbf{u} \quad (1)$$

Tidal forcing is applied at the open boundary and is described later in this section. Other environmental forcing such as that associated with wind stress could be included but are not considered here. A viscous term, proportional to viscosity,  $\mu$ , is included for numerical stability and may be space dependent. The equilibrium density is given by  $\rho_o$ ,

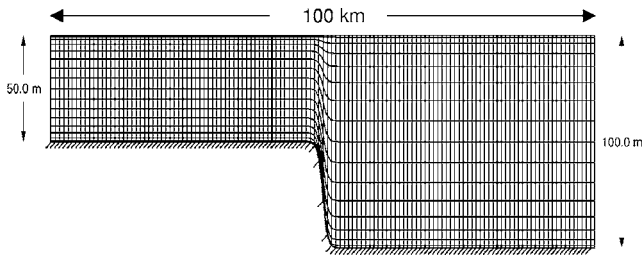


FIG. 1. Cross-range view of the terrain following coordinate system used to simulate a canonical shelf-break ocean environment. The acoustic field is computed over a 30 km range centered on the shelf break.

whereas the vector  $\mathbf{f} \times \mathbf{u}$  represents Coriolis acceleration. The advective derivative operator is defined by  $D/Dt \equiv \partial/\partial t + \mathbf{u} \cdot \nabla$ . The second term in this operator represents nonlinear interactions and is responsible for the generation of internal tides and solibores arising from tidal forcing. For incompressible fluids, the equation of continuity becomes

$$\nabla \cdot \mathbf{u} = 0. \quad (2)$$

Temperature and salinity fields are described by a pair of advection/diffusion equations, where

$$\frac{D\{T, S\}}{Dt} = \tau_{\{T, S\}} \nabla^2(T, S) \quad (3)$$

with the diffusivity defined by  $\tau_{\{T, S\}}$ ; the particular tracer is denoted by the subscript. The density field,  $\rho$ , is a function of space and time and it is related to temperature, salinity, and pressure distributions by an equation of state

$$\rho = \rho(T, S, p). \quad (4)$$

The IES-80 equation of state<sup>24</sup> is incorporated into this model to explicitly define Eq. (4). Together with a set of boundary and initial conditions, Eqs. (1)–(4) completely specify the fluid flow. The sound speed field  $c(\mathbf{r}, t)$  is a derived quantity, obtained from a phenomenological relationship<sup>25</sup> involving  $T$ ,  $S$ , and  $p$  once the previous set of equations are solved as a function of position for each time step. For computational purposes, the previous equations are mapped into an equivalent formulation treating the vorticity  $\xi = \nabla \times \mathbf{u}$  rather than the particle velocity.

For the example presented in the next section, 2D hydrodynamic computations are performed over a range of 100 km in water of variable depth, between a value of 50 m on the shelf and 100 m beyond the shelf break. The oceanographic grid represents a terrain following coordinate system and is shown in Fig. 1. Figure 1 represents a canonical shelf-break environment with a maximum slope of  $2.4^\circ$ ; the bathymetry is modeled in terms of a hyperbolic tangent function. The range step was fixed at 25 m, with the number of depth steps fixed at 65 for each range step. Because of the variable bathymetry and the cosine grid in the vertical, the depth resolution was dependent on range. Tidal forcing is implemented by applying a sinusoidal surface displacement at the right-hand boundary, with an amplitude of 2 m and a period of 12.4 h, with the latter corresponding to an M2 tidal cycle. The boundary conditions imposed on the environmental model are as follows. The model domain is closed on the

coastal (shallow) side,  $x=0$ , by a vertical wall, where the boundary conditions are  $u=0$ ,  $\partial v/\partial x=0$ ,  $\partial w/\partial x=0$ , and  $\partial \eta/\partial x=0$  with  $\eta$  representing the surface displacement. The boundary conditions on the open ocean side ( $x=100$  km) are, in addition to the tidal forcing given earlier, specified as  $\partial v/\partial x=0$  and  $\partial w/\partial x=0$ . No condition is imposed on  $u$  at the open ocean boundary. The vertical boundary conditions are  $\partial u/\partial z=0$ ,  $\partial v/\partial z=0$ , and  $\partial \rho/\partial z=0$  at the free ocean surface and bottom. For acoustic computations, a 30 km subset of this grid was chosen and centered on the shelf break. The sound speed field was interpolated to a rectangular grid for each time step prior to performing acoustic simulations.

### III. SIMULATION RESULTS FOR A SHELF-BREAK ENVIRONMENT

The shelf-break environment was chosen as an example to illustrate some features of acoustic field variability caused by tidally forced stratified flow over variable bathymetry. Some previously measured data is used for environmental initialization, but no effort is made to accurately model a specific shelf break region. For each environmental snapshot computed by the approach discussed in Sec. II, the sound speed distribution is processed through a wide-angle parabolic equation code incorporating a split-step Padé solver.<sup>26</sup> Assuming the environment is frozen for each snapshot, the acoustic field between 200–500 Hz is computed as a function of source depth and frequency over a 30 km range subset of the full 100 km environmental simulation, with the acoustic computational window centered at the point of maximum slope on the shelf break (see Fig. 1). Complex acoustic fields are then “stored” on vertical arrays located at selected ranges along this 30 km track.

A tacit assumption concerning the environment has been introduced here. For computational reasons we are effectively ignoring along-slope (i.e. out of plane) oceanographic variability. For many shelf-break regions, significant along-slope variations in both bathymetry and flow properties exist. Although fully 3D hydrodynamic computations of the environment and their effect on out-of-plane acoustic propagation are beyond the scope of this paper, we do consider a simplified scenario in Sec. III B 2 where azimuthal variations in the acoustic field are introduced in the following way. The 2D environmental snapshots are extended in the along-slope direction, mimicking a 3D shelf-break without along-slope oceanographic or bathymetric variability. The environment is therefore chosen to be invariant with respect to the along-slope direction, but the acoustic field can exhibit a dependence on azimuth. A wide-angle 3D parabolic equation<sup>27</sup> is then used to evaluate the azimuthal and time dependence of the acoustic field on vertical arrays located at a fixed radial distance of 10 km from acoustic sources placed at several locations near or in the shelf break region. The source frequency in this case is 100 Hz.

#### A. Sound speed variations caused by tidal forcing

Several environmental snapshots of the time-evolving sound speed environment and resulting acoustic transmission losses within the 30 km computation window are shown in

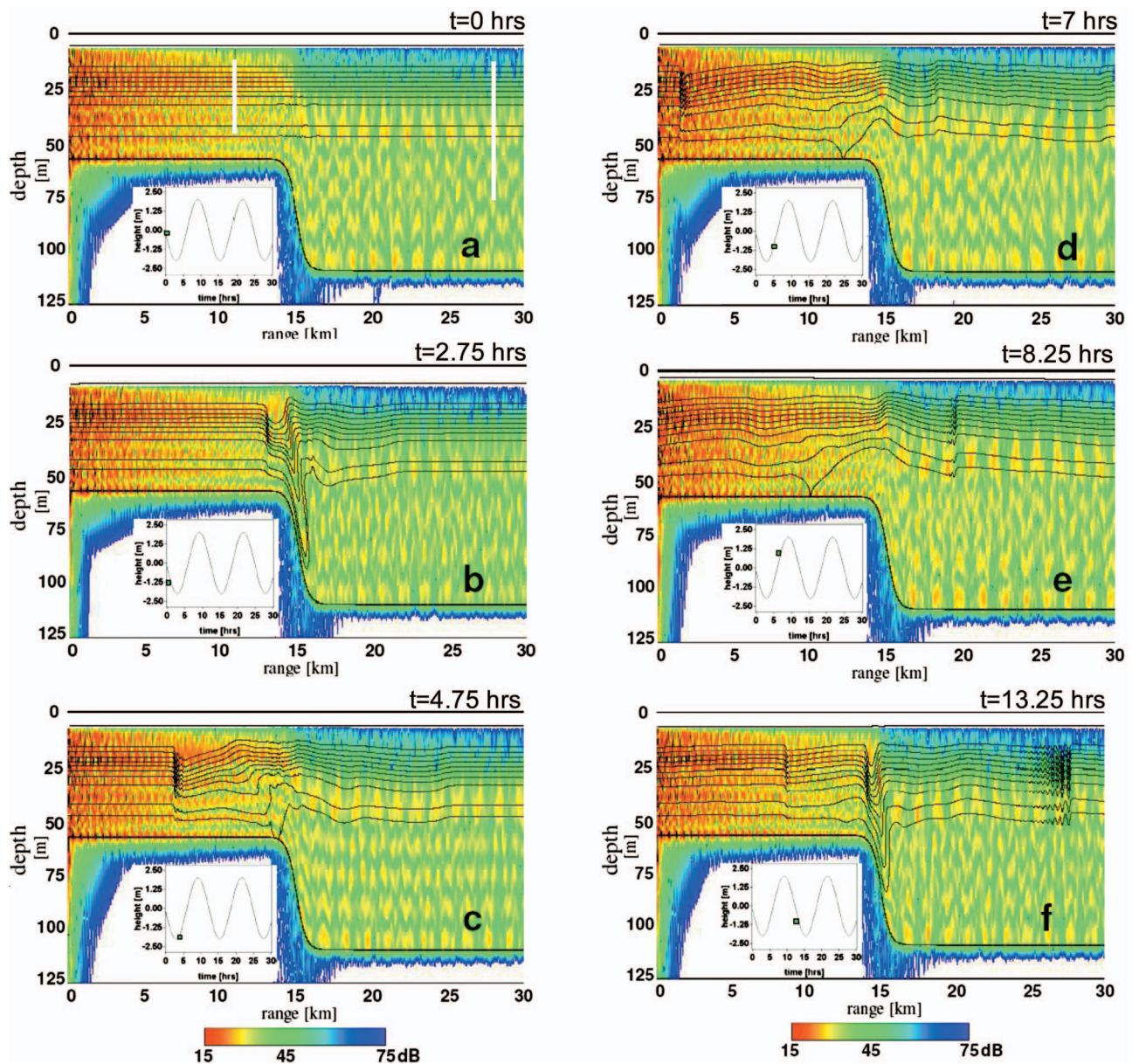


FIG. 2. Sequential set of environmental snapshots and associated transmission loss obtained over a period of approximately 13 h. For each, the inset shows the corresponding phase of the tidal cycle during which the sound speed field was computed. Sound speed is represented by the black contour lines, and initially ( $t=0$ ) corresponds to a range-independent summer profile. A thick black line at the top of each figure represents the maximum water height. The color overlays describe transmission loss at 400 Hz for a source at 15 m depth, located at the left edge of each picture. Geometric spreading is not included in the plots.

Fig. 2, which covers a 30 h time span [approximately 2.5 semidiurnal (M2) tidal cycles]. The environment in Fig. 2(a) corresponds to the starting sound speed distribution for the simulation, computed from the initial temperature and salinity distributions. The initial sound speed field is chosen to be range independent over the 30 km propagation track at time  $t=0$  h. The depth dependence of the sound speed represents a typical summer thermocline for the New Jersey shelf,<sup>1</sup> with a mixed layer of about 10 m below the surface and sound speed variations of approximately one percent from the surface to the bottom. The range independence of the sound speed field is not typical for this region; it is introduced here for simplicity in order to clearly illustrate the generation of internal tides and solibores without the additional complica-

tion associated with the existence of a range- and depth-dependent cold water pool that can extend out to the shelf break.

The fluid velocity is initialized to zero, corresponding to a quiescent ocean referenced to time  $t=0$  h. Tidal forcing is initialized as shown in the inset for Fig. 2(a), so that during spin-up the conditions corresponded to ebb flow. Choosing on-shore flow during spin-up results in a different transient sound speed response that eventually settles into a temporal sequence of environments similar to that described here. The thin black lines illustrated in the water column are sound speed contours, whereas the color coded overlays represent the acoustic transmission loss for a 400 Hz source located at the range origin ( $r=0$ ) and source depth of 15 m. The source

is fixed relative to the free ocean surface; this is equivalent to a configuration where the source is moored to a surface ship. Geometric spreading has not been included in Fig. 2. Bottom parameters (sound speed, density, and attenuation) are chosen to be average values typically found in the New Jersey Shelf, though range dependence in these parameters is ignored. Note that our purpose here is to illustrate the use of the model in a relatively simplified setting using reasonable parameter values, rather than to perform a detailed analysis of a specific environment. An analysis of specific environments will be pursued in future efforts. White vertical lines drawn in Fig. 2(a) locate the positions of the two vertical arrays which are used to process the simulated field data along a 2D range/depth slice. Array positions are fixed at 11 and 28 km from the source location. In Sec. III B 2, an alternative set of arrays are positioned at fixed range and variable azimuth with respect to sources placed near or within the slope-break region in order to investigate azimuthal field dependence in this environment.

As the barotropic tide continuously forces stratified water over the shelf edge, a significant vertical component of the buoyancy force develops at this location and acts as a local wave generation mechanism in which energy is radiated away from the shelf break. This energy is predominantly in the form of an internal tide, illustrated in Fig. 2(b), where an internal tide has recently formed and moved onto the shelf. It is located at a range of about 13 km from the source and is traveling shoreward. The sound speed contours indicate that the temperature has been advected downward at the shelf break during this time. A few hours later, Fig. 2(c) shows that the internal tide has progressed about 7 km shoreward and developed oscillations on the trailing edge, indicating a transformation of the internal tide to a solibore with a depth dependence dominated by the first internal wave mode. A few hours later, the solibore has continued to propagate toward the acoustic source and upwelling is observed over the shelf break [Fig. 2(d)]. As time progresses another internal tide has formed, begun to transform into a solibore at a range of about 20 km and moves seaward [Fig. 2(e)]. This solibore continues to add oscillations as it progresses seaward [Fig. 2(f)]. A solibore is also seen at a range of about 8 km traveling shoreward and another internal tide is beginning to form over the shelf break at a range of approximately 14 km. A detailed analysis of the ocean dynamics for a qualitatively similar environment is given in Ref. 15 in which a rigid lid, rather than a free surface model, is used to simulate internal wave generation. Changes in water depth caused by free surface movement in response to tidal forcing are viewed most clearly by comparing Figs. 2(b) and 2(e), where the thick black line at the top of each figure represents the upper limit of the water height. Note that tidal waves have wavelengths on the order of  $10^2$  km, the length of the computational domain. Over the 30 km range for the acoustic computational grid, the dominant effect of the tide is to raise or lower the water column height uniformly as a function of time. Small scale surface waves would cause spatially local water depth variations over short time intervals, but the parabolic equation code used for the acoustic calculations cannot handle those variations directly. An alternative implementa-

tion of the parabolic equation<sup>28</sup> could be used to include small scale surface waves, but the inclusion of the corresponding hydrodynamic component over the domain of interest would be computationally prohibitive.

## B. Acoustic field variability caused by tidal forcing

### 1. Acoustic response along a range/depth slice

The transmission loss patterns in Fig. 2 are indicative of time dependence in multi-mode propagation. The patterns themselves are determined by several factors such as (1) the source depth and local environment at the source which determines the initial modal distribution of energy, (2) tidally induced modulation of water depth which can introduce or cut off a mode or modify the relative phasing between modes, and (3) volume variability associated with the internal tides and wave packets induced by tidal forcing. Since these factors are coupled together through tidal forcing, it is difficult to separate out the individual contributions to the overall temporal and spatial evolution of the transmission loss pattern.

In order to quantify variability in the acoustic field, the vertical arrays [cf. Fig. 2(a)] are used to process the simulated field data. They span water depths between 7.5 and 40 m at the shallow array site, 7.5–80 m at the deep site. Both the acoustic source and the arrays were assumed to be moored from surface ships; as the free surface moves in response to the tide, the source and array depths remain fixed relative to the surface but change relative to the fixed bottom. Two time windows, A and B, with durations of 30 min each are selected from the 30 h simulation. The complex pressure  $P(r, z, t, \omega)$  at frequency  $\omega/2\pi$  is recorded on each hydrophone every 20 s within a window, for a total of 90 complex acoustic field vectors per array for each window. The frequency band for the acoustic field computation was  $200 \leq \omega/2\pi \leq 500$  Hz, where acoustic computations are performed with a 1 Hz resolution across the band yielding a total of 54,000 field vectors. The starting time for window A corresponds to the environment in Fig. 2(d), whereas the starting time for window B corresponds to the environment in Fig. 2(f). Window A is representative of an environment where a solitary wave packet passes through the acoustic source position, changing the local sound speed distribution near the source, while window B describes a situation where a packet crosses the array located 28 km from the source and the local source environment is approximately time independent. In both cases, the sound speed field between the source and the array is space and time dependent. Within each window a function  $\Gamma(\omega, t, t_0)$ , defined below, is computed for  $t_0 \leq t \leq t_0 + \Delta$  at frequency  $\omega/2\pi$ , where  $t_0$  is the reference starting time for evolving the environment in window A or B, and  $\Delta$  is the window width of 30 minutes.

Let  $e(\omega, t_0)$  represent a “ground truth” vector of complex pressure fields,  $[P(r, z_1, t_0, \omega) \dots P(r, z_N, t_0, \omega)]^T$  received on a vertical array of  $N$  phones at time  $t_0$  during either window A or B, and let  $f(\omega, t)$  represent a replica vector of complex pressure fields on the same array at time  $t \geq t_0$ . Then  $\Gamma(\omega, t, t_0)$  is defined by a ratio of inner products given by

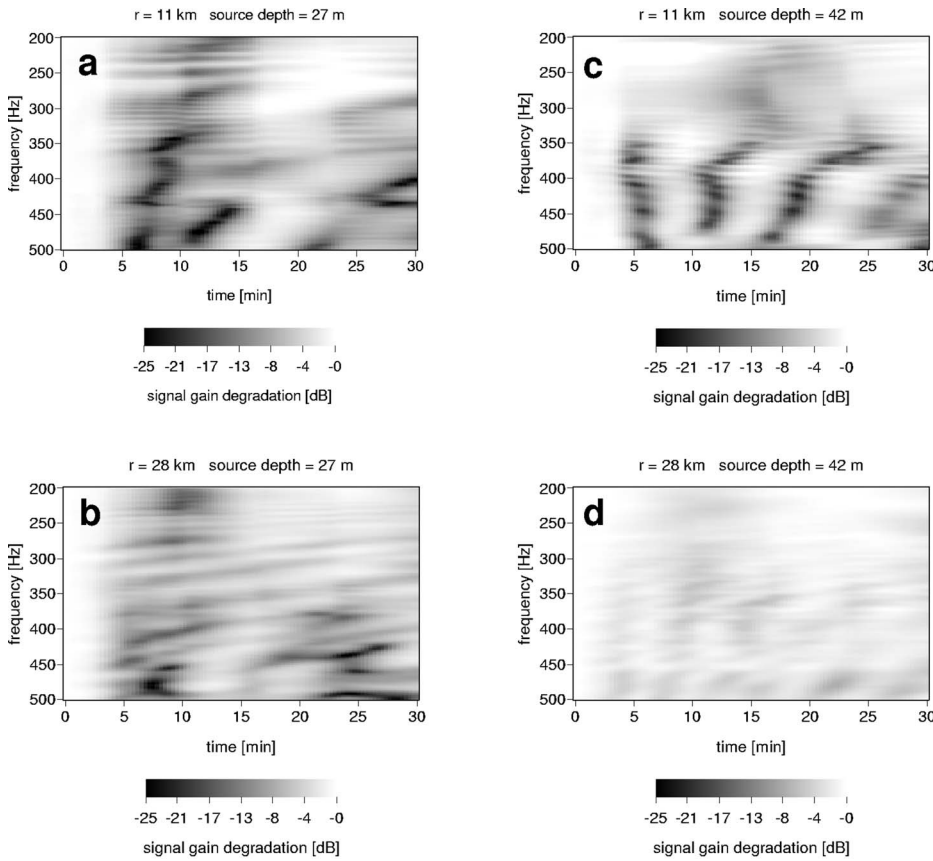


FIG. 3. Signal gain degradation computed from Eq. (5) as a function of frequency and time during window A, for two source depths (27 and 42 m) and two array locations (11 and 28 km). The degradation was computed with a free ocean surface.

$$\Gamma(\omega, t, t_0) = \frac{|e^* \cdot f|^2}{|e^* \cdot e|^2} = \frac{|f(\omega, t)|^2}{|e(\omega, t_0)|^2} \cdot |\hat{e}^*(\omega, t_0) \cdot \hat{f}(\omega, t)|^2 \quad (5)$$

with the caret denoting a unit vector and an asterisk representing the conjugate transpose. Equation (5) is useful for the assessment of array performance in a time-varying medium, and can be interpreted as a measure of signal gain degradation within the time window. It provides an estimate for the period in which a measured field could be used as a replica in a linear matched field processor before the peak power degrades significantly. The middle equality in Eq. (5) then represents the matched field processor power relative to the expected power. Algebraic manipulation yields the second line of Eq. (5), separating the total degradation associated with the full complex field into the product of its individual amplitude and phase contributions, respectively.<sup>29</sup> Signal gain degradation, in the form  $10 \log \Gamma$ , is discussed below for the important case of propagation under tidally driven stratified flow. We note here that in the next subsection a different interpretation is given for the vectors  $e$  and  $f$ , and Eq. (5) is then interpreted as a temporal correlation coefficient measured across the array aperture.

Several plots of signal gain degradation (SGD) are given in Fig. 3 for results obtained by propagation through the 30 min sequence of environments associated with window A. The images are presented as functions of time and source frequency (200–500 Hz band) at two source depths (27 and 42 m) for each of the two arrays. The frequency-time degradation patterns reveal significant complexity, even for this relatively simple environment. Representing the full degradation (i.e. a combination of amplitude and phase contribu-

tions), they show that over the first 2 to 3 min the SGD is less than about 2 dB while for times greater than about 3 min, the SGD is usually (but not always) significantly larger with considerable variation as a function of frequency and time. The increased degradation after a few minutes implies mismatch (i.e., temporal decorrelation) between the signals  $e$  and  $f$ . Temporal correlation of narrow-band signals that fall within this frequency band has been measured<sup>30,31</sup> and modeled<sup>5,32,33</sup> in shallow water environments exhibiting significant internal wave activity, and full field correlation times on the order of two or three minutes are typical. The correlation times determined in those studies were found to be mode dependent, with the first mode tending to have the longer correlation time since its major contribution to the field as a function of depth spans a vertical region below the thermocline and is less susceptible to sound speed perturbations in the upper part of the water column.<sup>5</sup> The measured values are consistent with the results shown in Fig. 3. For acoustic propagation in the 200–300 Hz band, Fig. 3(a) shows a clear recorrelation of the field after about 15 min. To a somewhat lesser extent, a similar effect is seen in Figs. 3(b) and 3(d) for different frequency bands and time slices within the window. Within the 350–500 Hz band, Fig. 3(c) displays a comparatively stronger recorrelation and also shows a temporally periodic degradation structure. Partial recorrelation of the field has been noted in the SWARM95 data and interpreted as a periodic feature occurring when the relative phase retardation between dominant mode pairs approaches  $2\pi$  radians.<sup>33</sup> With the exception of Fig. 3(d), these plots indicate that the degradation is enhanced as the packet passes

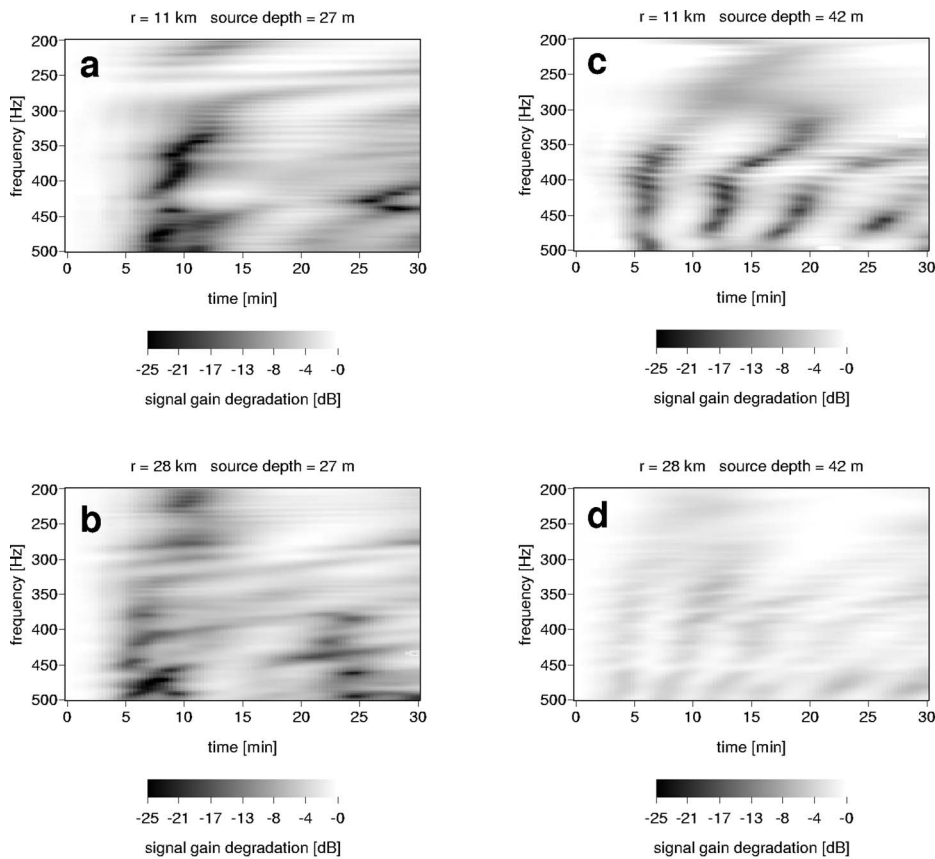


FIG. 4. Signal gain degradation computed as in Fig. 3, but with a fixed ocean surface.

over the source position, a result discussed by several authors<sup>3,5</sup> using simple internal wave models. The result here is more complex and difficult to interpret as the environment changes along the entire propagation path, whether a solitary wave packet is present or absent.

Results from a number of studies support the view that the frequency and time dependence of the degradation illustrated in Fig. 3 is likely caused by a combination of several time dependent effects linked to tidal flow: mode coupling along the acoustic track,<sup>2-5</sup> water depth variation<sup>34,35</sup> and redistribution of modal energy at the source.<sup>2-5</sup> The first effect is an indirect consequence of the stratified flow over variable bathymetry, which induces range and time-dependent internal wave perturbations of the mean sound speed field. While a conclusive analysis using modal decomposition is beyond the scope of this paper, previous work has shown that mode coupling is a function of both acoustic frequency and the range gradient of the resulting sound speed perturbations. It alters both the particular modes received at the array and their relative phase relationships,<sup>2-5,7</sup> so that mismatch between temporally separated signal transmissions is expected to occur. Water depth variations due to tidal flow can modify the mode distribution and phasing between modes, possibly by introducing a new mode or eliminating a mode that falls below cutoff. Over the particular short duration time windows considered in this example, water depth changes due to the tide have a small effect on SGD as discussed below, but over a longer time scale (hours) it can be more significant.<sup>34,35</sup> The third effect is that the local sound speed distribution in the immediate vicinity of the source changes due to sound speed perturbations passing through the region,

and this local environment determines the mode distribution excited by the source.<sup>2,3,5</sup> This distribution, in conjunction with bathymetric variation and mode coupling in the water column, can play a significant role in determining the energy distribution at the receiving arrays.

An attempt is made here to assess the relative importance on SGD of individual contributions of both tidally induced water depth variations and internal wave induced sound speed perturbations. A separate set of acoustic simulations are performed in the environment described previously, except that for these field computations the water depth is held fixed throughout the time window using the water depth present at time  $t_0$ . This case represents a situation where tidally induced water depth changes are ignored but volumetric sound speed perturbations caused by the tide are included. Examples of signal gain degradation under this constraint are shown in Fig. 4 for time window A. Comparing Figs. 3 and 4 one can detect small differences in degradation that can be attributed to changes in water depth. These depth variations are quite small, approximately 0.3 m over each of the 30 min time periods, and weakly alter the temporal variation of SGD in selected frequency bands. It is clear, for example, that most of the roughly periodic structure of the degradation above 350 Hz in Fig. 3(c) is primarily, though not exclusively, due to volume variability since the corresponding plot without surface variation [Fig. 4(c)] shows similar behavior. The effect on degradation of changing water depth is more significant for propagation on the shelf for the shallow source depth [Fig. 4(a)], probably due to the fact that the percentage change in water depth is about twice that found at the array located 28 km from the source.

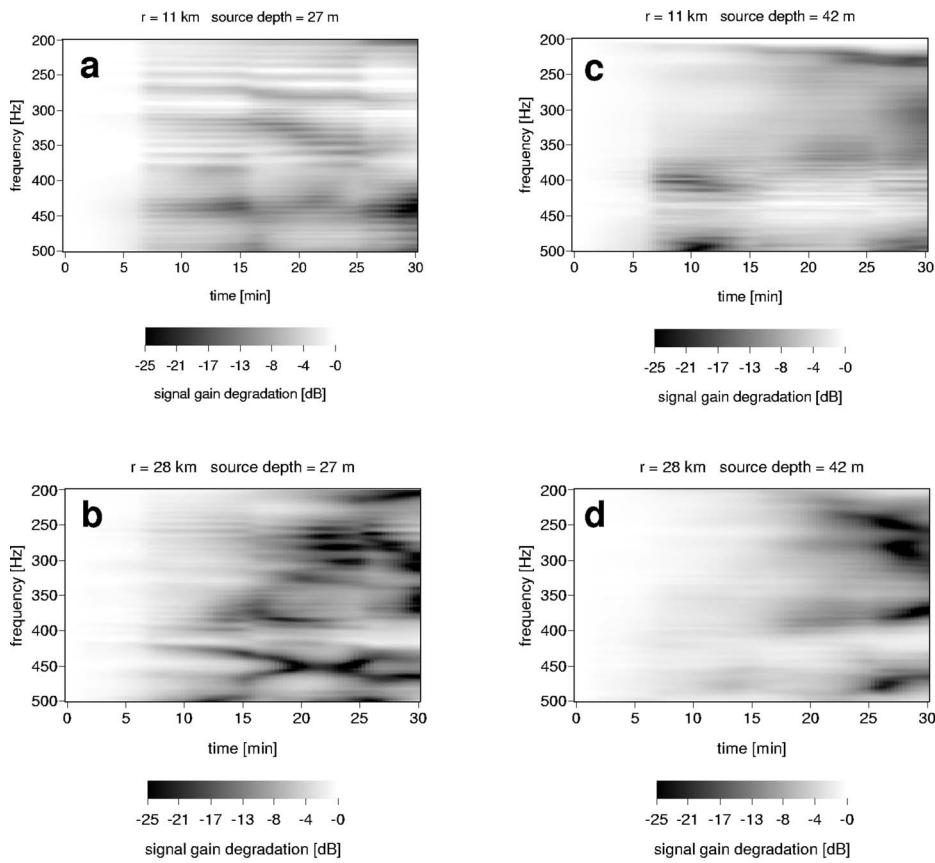


FIG. 5. Signal gain degradation for window B, computed with a free ocean surface.

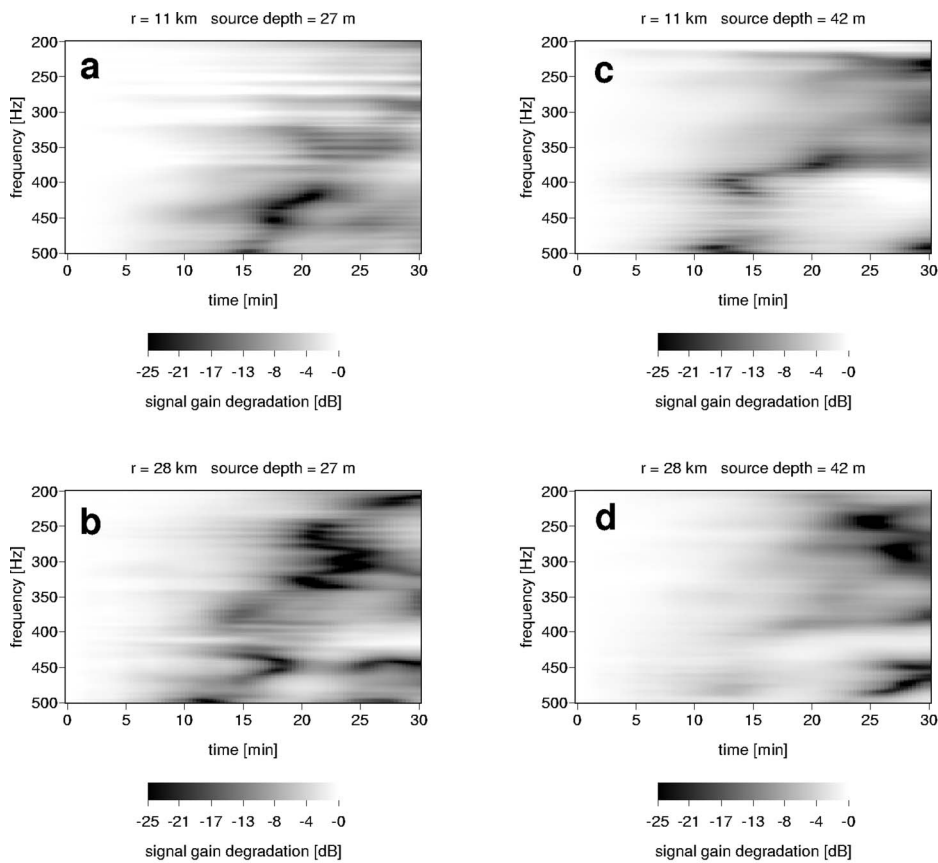


FIG. 6. Signal gain degradation for window B, computed with a fixed ocean surface.

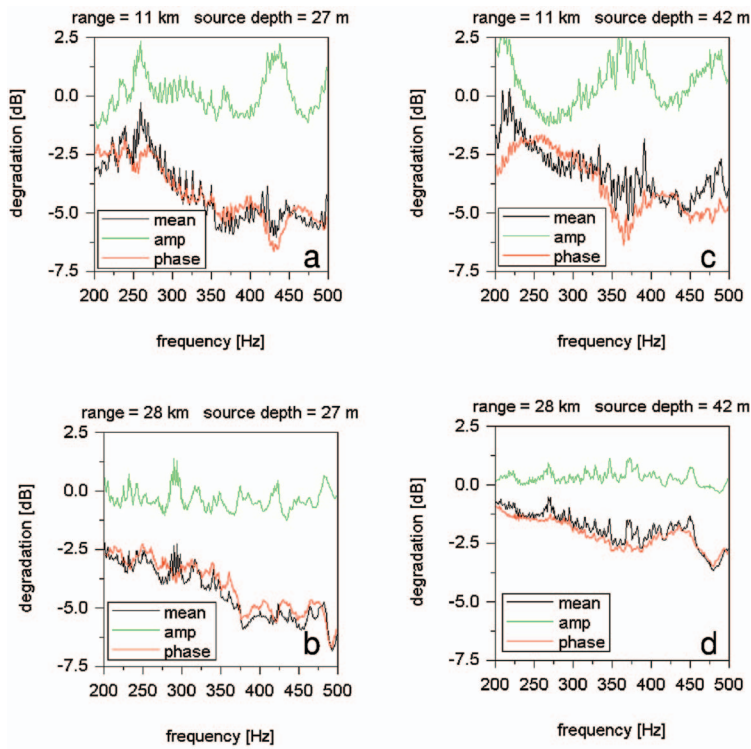


FIG. 7. Decomposition of signal gain degradation into amplitude and phase contributions for window A, computed with a free ocean surface.

Similar comments can be made for both the (full field) SGD plots shown in Fig. 5, which correspond to the evolving ocean environment in window B, and the associated fixed water depth case illustrated in Fig. 6. Again, there are small differences between the corresponding fixed surface/free surface degradation plots for most time-frequency regions, indicating the SGD is primarily caused by volume variability for short time windows. As was the case for the sequence of snapshots in window A, the most significant acoustic

changes occur for the array located on the shelf. The environmental conditions along the track are quite different for window B relative to those in window A. For window B there is significant downwelling [Fig. 2(f)] that is not present in window A [Fig. 2(d)]. In addition, a large solitary wave packet crosses the receiving array during time window B. The full field degradation in Figs. 5(c) and 6(c) are strikingly different from the corresponding SGD computed with the environment in window A. Note that because the environ-

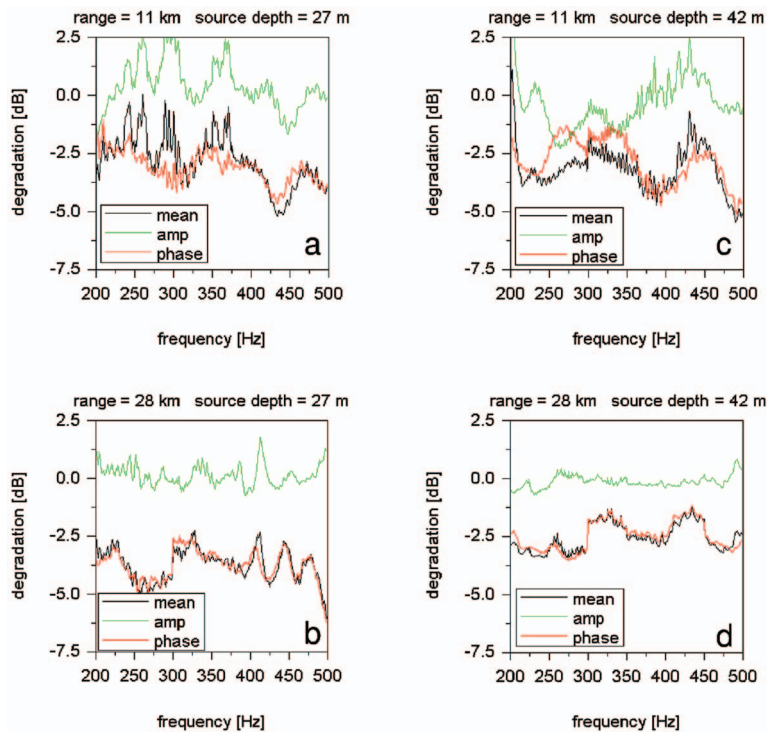


FIG. 8. Decomposition of signal gain degradation into amplitude and phase contributions for window B, computed with a free ocean surface.

mental dynamics is nonstationary, some caution should be applied in extrapolating these results to arbitrary time windows during different phases of the M2 tidal cycle.

It is well known that phase fluctuations dominate variability in both transmission loss and field coherence. For example, measurements of array gain degradation for data acquired on the New Jersey shelf are consistent with the prediction that phase contributions dominate the degradation.<sup>29</sup> Results illustrated in Figs. 3–6 are consistent with phase dominance, a conclusion drawn from a direct comparison of frequency-time SGD plots for the individual amplitude and phase contributions obtained through Eq. (5). Instead of presenting those figures, this result is illustrated here in an alternative format by averaging the individual contributions to degradation over the time windows for each acoustic frequency. The results are shown in Fig. 7 corresponding to window A and Fig. 8 corresponding to window B. The black curve in each of these plots, labeled “mean,” describes the full field calculations. For most frequency components, the trend is that the (full field) mean degradation follows the phase contribution. The trend is more closely followed for the longer range transmission (28 km), likely due to the relative importance of the gradual accumulation of phase shifts that occur as the acoustic field passes through small perturbations in sound speed over a longer propagation path. Similar trends are seen for the fixed surface cases (not shown), implying that the phase degradation is primarily due to volume variability.

An example is now presented which demonstrates how a representative sonar problem, that of detection range estimation, is affected by both tidal height variation and internal waves. Sound from a source located at 50 m depth and 15 km range seaward from the break is propagated directly up slope to receivers sampling the field at ranges between 20 and 30 km from the source. Detection range,  $r_d$ , based on a figure of merit FOM=66 dB is computed as follows. For the purpose of smoothing the data, a set of depths, ranges, and frequencies are included. The acoustic intensity is computed and averaged first over a 50 Hz bandwidth (in 1 Hz increments) starting at  $f_0$ , and then averaged over a 10 m square (20–30 m in depth and 10 m in range starting at  $r_0$ ). Explicitly, the mean intensity is defined by

$$\bar{I} = \int_{r_0}^{r_0+10} \int_{20}^{30} \int_{f_0}^{f_0+50} \frac{I df dz dr}{10^2 \times 50}. \quad (6)$$

The spatially and frequency averaged TL is then given by  $\overline{TL} = 10 \log_{10} \bar{I}$  for each time  $t$  in hours. The detection range is the range at which the TL crosses the FOM. However because  $\overline{TL}$  is not strictly decreasing,  $\overline{TL} = \text{FOM}$  at several ranges,  $r_{d,n=1,2,\dots}$  so that the detection range  $r_d(t)$  is defined here as the average of the  $r_{d,n=1,2,\dots}$  at time  $t$ . This also permits the use of the standard deviation  $s_d(t) = \sigma(r_{d,n})$  to measure the spread of detection ranges. Finally, the time correlation gives a quantitative measure of how two time series vary simultaneously, for example,  $\langle h_t, r_d \rangle = \int_0^{\max} \tilde{h}_t(t) \tilde{r}_d(t) dt$  where the tilde indicates that the tidal height,  $h_t$ , and  $r_d$  are both zero mean and normalized. Because of the tidal variation, the bathymetry  $b(r, t) = h_t(t)$

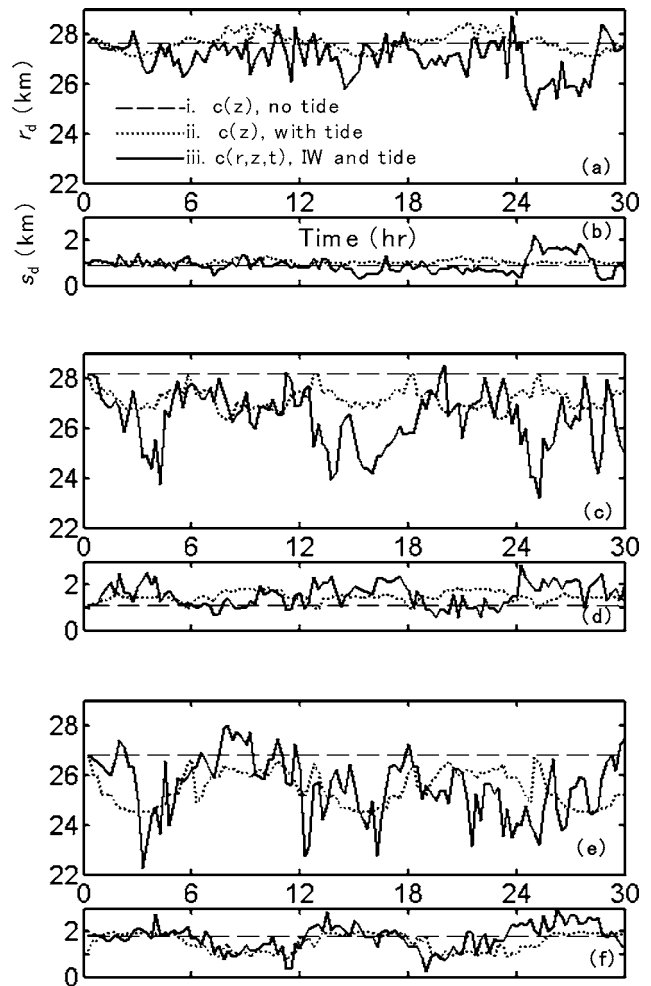


FIG. 9. Detection range estimates,  $r_d$ , and detection range variances,  $s_d$ , obtained over a 30 h time window as functions of acoustic frequency. (a,b)  $r_d, s_d$  for the 200–250 Hz band, respectively; (c,d) same quantities computed for the 300–350 Hz band; and (e,f) same quantities computed for the 400–450 Hz band.

$+b_0(r)$ , where  $b_0$  is the bathymetry at  $t=0$ . Figure 9(a) shows  $r_d$  for the 200–250 Hz band corresponding to three different cases: (i) the perfectly stratified sound speed distribution  $c(z)$  without tidal variation (dashed line corresponding to the environment at  $t=0$  h), (ii) the same sound speed profile,  $c(z)$ , but including only tidal variation  $h_t$  (dotted line), and (iii) inclusion of both internal waves and tidal variability  $c(r, z, t)$  (solid line). In case (ii)  $c(z)$  is required in the interval  $0 \leq z \leq b(r, t)$  for each  $r$  and  $t$ . In fact, it is known for  $z \leq \max_{r,t} [b(r, t)]$  and is truncated at  $b(r, t)$  as needed. All cases match at  $t=0$ , but  $r_d$  in case (ii) demonstrates a strong correlation with tide  $\langle h_t, r_d \rangle = 0.88$ , with minima during low tide and maxima at high tide. Case (iii) is much more variable in Fig. 9(a) and has no strong single frequency component, from the Nyquist period to the inertial period, 0.5–17 h. The significant decline in  $r_d$  between 24 and 28 h is due to simultaneous upwelling on the seaward side of the break and downwelling on the shallow side. Internal waves tend to reduce detection range relative to case (ii), by 1–2 km for 200–250 Hz. The standard deviation over the 200–250 Hz

band for case (iii) in Fig. 9(b) also shows an increase over the same period. Otherwise,  $s_d$  in both cases (ii) and (iii) indicate no significant periodicity and are usually predicted by the time constant case (i). Results for the detection range within the 300–350 Hz band are illustrated in Fig. 9(c). Case (ii) shows the maxima in  $r_d$  occur at mean tide, the minima occur at both high and low tide and the standard deviation in Fig. 9(d) indicates similar variation, but inverted. These variations are closely correlated to the absolute deviation of the tide from the mean,  $\langle |h_t|, r_d \rangle = -0.82$  and  $\langle |h_t|, s_d \rangle = 0.81$ . The variability of  $r_d$  for case (iii) is only partially correlated to tide with  $\langle h_t, r_d \rangle = 0.43$ , although the standard deviation is anticorrelated with a slightly higher magnitude,  $\langle h_t, s_d \rangle = -0.59$ . The detection range in this band is markedly reduced during upwelling/downwelling events in the intervals of 3–4.5, 12.5–13, 15–16.5, 24.5–25.5, and 28–29 h. It is observed at those times that the TL increases because of the energy being scattered into the bottom. The wavelengths in this band are particularly susceptible to this loss mechanism due to the particular combination of distance (in range) between up and down displacements of the thermocline, magnitude of those displacements and their relation to the break. These combinations occur briefly, but regularly, so that the reductions in  $r_d$  are more frequent and of shorter duration than the reduction of  $r_d$  in the 200–250 Hz band. The internal waves can reduce detection range up to 5 km relative to the case (ii). In Figs. 9(e) and 9(f), describing the 400–450 Hz band, the result for case (ii) indicates that the  $r_d$  and  $s_d$  are very closely correlated to tidal height with  $\langle h_t, r_d \rangle = 0.82$  and  $\langle h_t, s_d \rangle = -0.91$ , respectively. For case (iii) in Fig. 9(e), the detection range correlation to tidal variability is lower than in the 300–350 Hz band; the most significant periodic component is centered at 10.2 h, rather than the M2 tidal period of 12.4 h, but the standard deviation shows moderate anti-correlation to tide,  $\langle h_t, s_d \rangle = -0.60$ . The reductions in  $r_d$  for this band occur at virtually the same times as for 300–350 Hz, during the same upwelling/downwelling events. Case (ii) is much more variable in this frequency band, with  $r_d$  varying up to 3 km, so that case (iii) only reduces  $r_d$  by another 3 km. In summary, higher frequencies show greater decreases in detection range due to tidal variability (up to 2 km over a 30 h time window) and internal waves (an additional 5 km decrease). Also, whereas the tidal height can be used to predict variation in  $r_d$  and  $s_d$  for a given frequency when  $c(z)$  is time independent, the introduction of internal waves indicates that detection range is also dependent on the location and size of the internal waves, often without any discernable periodicity.

## 2. Azimuthal dependence of the acoustic field

The acoustic results discussed earlier were obtained for a single range-depth slice during periods when there were qualitatively different environments between the source and receiving arrays. Some examples of the azimuthal dependence of the acoustic field on tidally driven stratified flow in a shelf-break region are considered below. A simple exten-

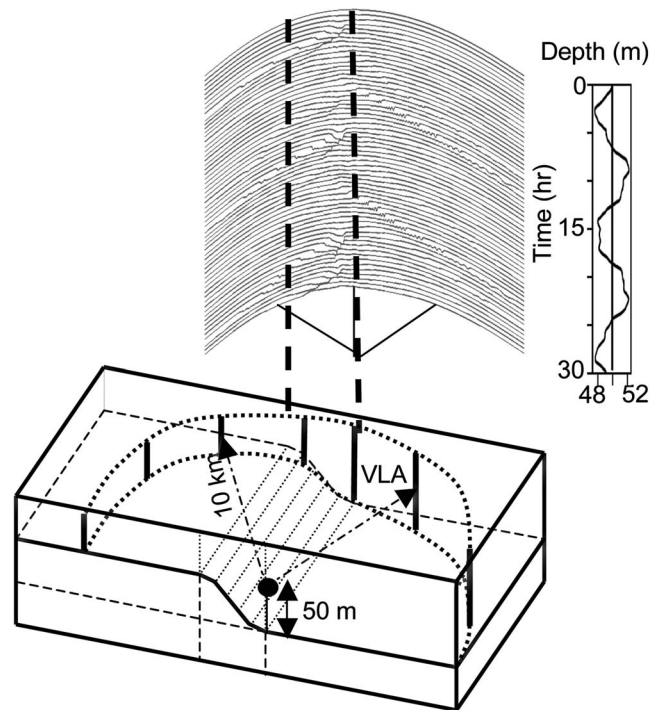


FIG. 10. Source/receiver configuration for 3D simulations of the acoustic field under tidally driven, stratified flow. The source is shown here at the bottom of shelf break and 50 m above the bottom, though results in Figs. 11 and 12 also consider the source positioned in the shelf-break or just at the top of the shelf-break region. The waterfall plot illustrates the azimuth-time distribution of the 1500 m/sec iso-speed contour at a depth of 25 m and using 0.5 h updates. To the right of the waterfall plot is the time signature of the temporal variations in water column depth for the same period is shown. Dotted vertical lines denote the boundaries of the shelf-break region.

sion of the 2D environmental model discussed in Sec. II is made in the along-slope direction (projecting out of the page in Fig. 1). This results in a 3-D shelf-slope region for which both the sound speed field and bathymetry are invariant in the along-slope direction. However, acoustic propagation through this environment exhibits significant azimuthal variability. To illustrate the azimuthal dependence on the acoustic field, a set of 721 vertical arrays is placed on a circular arc within, or adjacent to, the shelf-break region. An example of a source-receiver configuration in this extended environment is depicted in Fig. 10, along with an azimuth-time waterfall display of the 1500 m/s isospeed contour which is located at a depth of approximately 25 m. The arrays span  $180^\circ$  of azimuth and are located at a range of 10 km from bottom moored acoustic sources; these sources are placed in or near the break at midwater depth. The vertical arrays are positioned along the arc in one-third degree azimuthal increments, and extend from the bottom to 10 m below mean water depth. In Fig. 10, the source is located just seaward of the shelf-break and its depth is 50 m from the bottom near midwater depth. A graph of the temporal variation of the water depth on the shelf during a 30 h time period is also displayed in Fig. 10, aligned along the vertical (increasing time) direction of the waterfall plot. The vertical dotted lines delineate the boundaries of the shelf break. This waterfall plot shows a number of internal waves, generated at the shelf break, and radiating out from this region.

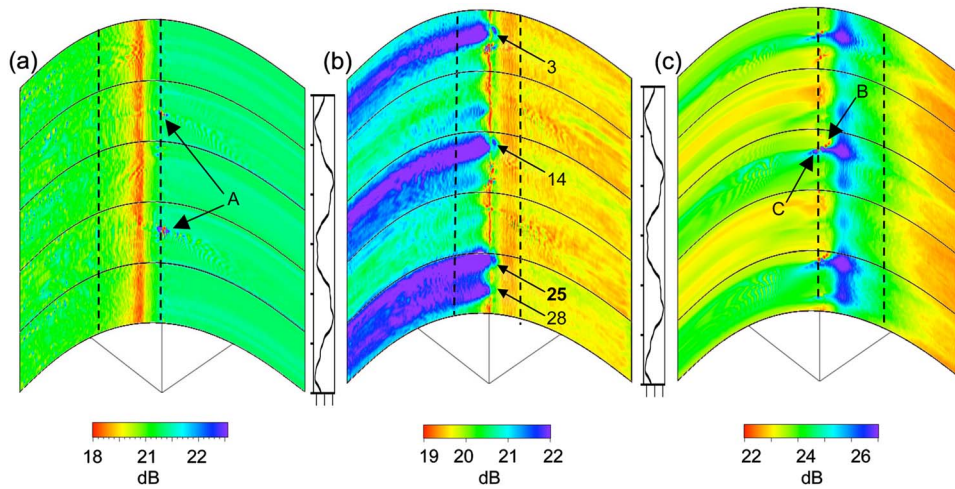


FIG. 11. (Color online) Plots representing depth-averaged transmission loss at 100 Hz, computed over each vertical array located along a 180° circular arc at a range of 10 km from an acoustic source. Results are presented as a function of azimuth and time for three source locations: (a) source at bottom of shelf-break (b) source at midbreak and (c) source at top of shelf break. Dotted vertical lines delineate the shelf-break boundaries. Several features at  $t=3, 14, 25,$  and  $28$  h are indicated by the numbered arrows in (b). Similar features appear in (c) though are not numbered.

With Fig. 10 as a reference for the general source-receiver configuration and time evolving environment, the depth-averaged transmission loss over each array is computed at 100 Hz as a function of azimuth and time. The averaged loss is presented in Fig. 11 for three source locations and midwater depths: (a) source at the bottom of the shelf-break, 50 m above bottom, (b) source at midbreak, 38 m above bottom, and (c) source at the top of shelf-break, 25 m above bottom. Note that the scales for each figure are different. The set of parallel curves for fixed times and variable azimuth in Figs. 11(a)–11(c) indicates the time of mean water depth during the 30 h simulation period. The vertical dotted lines again delineate the boundaries of the shelf-break region for the three source positions (the plots are shifted for each source location). Although the bathymetry largely determines the spatial distribution of the transmission loss, some features of the loss can be credited to solibores or other tidal flow induced sound speed variations. The most significant feature of the azimuth-time plot of transmission loss in Fig. 11(a) is the strong focusing located at about midbreak, due to horizontal refraction of acoustic energy along the slope. The levels have weak time dependence in the focusing region, but show little evidence of a tidal signature in this plot. Strong loss is seen at locations labeled A, just seaward of the shelf-break and is associated with significant downwelling of warm water along the propagation path that leads to solibore evolution in deep water. The loss plot for the source at midbreak [Fig. 11(b)] illustrates quite different behavior. In the shallow region (to the left of the dashed lines delineating the shelf break), loss varies approximately with temporal variations in water depth, with higher mean loss at low tide and lower loss at high tide. However, each of these variations in loss is also associated with downwelling over the break [cf. Fig. 2(b)], with the latter generating internal waves in shallow water (cf. Fig. 10). There are four maxima in the transmission loss, occurring at 3, 14, 25, and 28 hours. In particular, during the last low tide from 24 to 30 hr, the loss reaches a maximum twice, at about 25 h (which, notably, precedes tidal minimum) and 28 h. Both times are associated with strong downwelling events at the break. Within the shelf-break region a narrow azimuthal sector exhibits strong, but highly time variable focusing along the isobath

under the source. The focusing is weakest at exactly the same times of higher loss in shallow water, with superimposed shorter period variation of perhaps 3 h. Each reduction can be associated with downwelling. The source is at a fixed distance from the bottom, but the local change in the sound speed profile alters the relative excitation of the modes; it is the likely candidate for the periodic temporal variations in the loss. In particular, downwelling of higher sound speed water to a position below the source depth would lead to lower excitation of the lowest order modes. At the deep end of the shelf break, a broader but relatively time invariant focusing region is present. For a source located above the top of the break at a depth of 25 m [Fig. 11(c)], the propagation exterior to the break region also shows lower intensity during the same time periods as in Fig. 11(b). Indeed, the shadow region at 25 h, which precedes lowest tide but has very strong downwelling, is more intense than at 28 h, which is the low point of that tide. There is also time coincident fading at all azimuths, strongly suggesting reduced source excitation of propagating modes. Additionally, there is focusing (arrow B) and shadowing (arrow C) in the shallow region due to internal wave/bores generated at the shelf break. Along the center of the break, horizontal refraction due to the sloping bottom creates a shadow region, with deeper shadows at the same times as noted earlier.

The relative influence of tidally induced water depth variations and volumetric sound speed perturbations on the azimuthal dependence of the acoustic field is considered next. Fig. 12 shows three sets of paired azimuth-time images which are computed with a generalization of Eq. (5). The modification allows for azimuthal variation of the field, i.e.,  $\Gamma(\omega, t, t_0, \theta)$  where  $0^\circ \leq \theta \leq 180^\circ$ . There is one pair of images for each of the source locations. For pair (a,b) the source is positioned at the bottom of the shelf, the source is located at midbreak for pair (c,d) and in pair (e,f) the source is located at the top of the break. The pressure field vectors  $\mathbf{e}$  and  $\mathbf{f}$  on each vertical array now have somewhat different meanings than those given in the previous subsection. Here we interpret Eq. (5) on each array as a temporal correlation between pairs of acoustic field vectors defined as follows. For the first image of each pair [Figs. 12(a), 12(c), and

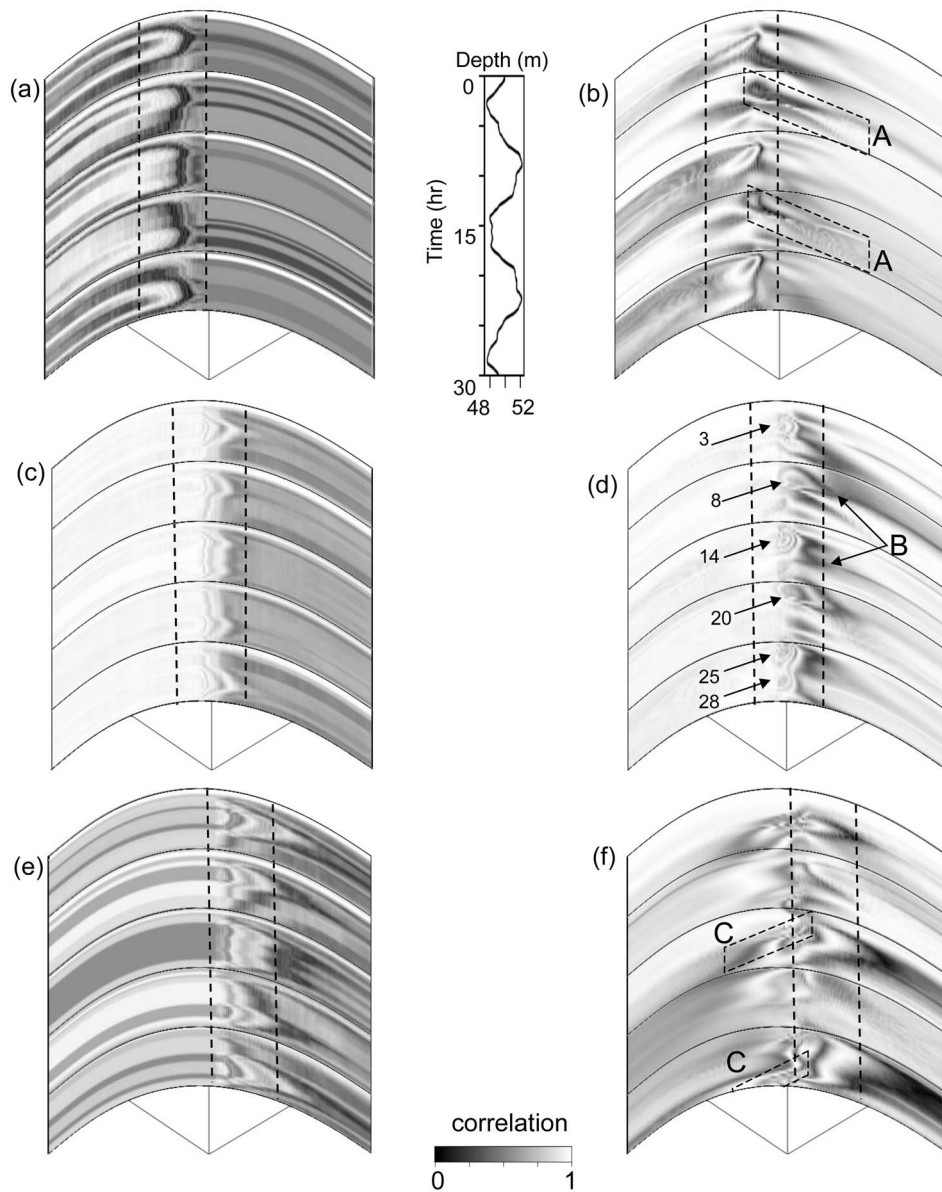


FIG. 12. Azimuth-time correlation plots at 100 Hz, computed over each vertical array located along a 180° circular arc at a source/receiver range of 10 km. There are three sets of paired images, one pair for each source location. The correlated fields displayed in each are discussed in the text. For (a,b) the source is positioned at the bottom of the shelf; in (c,d) the source is located at mid-break; and in (e,f) the source is located at the top of the break. Labeling in (d) is similar to that in Fig. 11(b), and indicates time in hours.

12(e)], the vector  $f$  now represents the acoustic field on an array at fixed time  $t=0$  h, corresponding to the starting environment in Fig. 2(a). The vector  $e$  is now chosen to describe the time evolving acoustic field on an array for the same initial environment though, for  $t>0$ , the water depth is allowed to change due to tidal variations over the full 30 h period of the computation. Therefore, the correlation between the two pressure vectors in this case depends only on variability in the water column displacement linked to tidal variations and the fields re-correlate perfectly each time the tidal variation passes through the mean height at  $t=0$ . This does not preclude shorter periods of variation seen on each of these plots, especially Figs. 12(a) and 12(e). No volumetric variations (internal tides and solibore) are included. Note that away from the break, the azimuthal variation is weak or vanishing in Figs. 12(a), 12(c), and 12(e) as the bottom is flat. The correlation in these plots varies significantly, from uniformly near unity in the shelf region of Fig. 12(c) to almost zero at points in the break region of Fig. 12(a). Generally the strongest variation in this set occurs when the propagation

path transverses the entire break as on the shelf in Fig. 12(a) and seaward in Fig. 12(e). The second image of each pair, Figs. 12(b), 12(d), and 12(f), describes the field correlation between the same tidally generated variations of the first image (specified by  $e$  above) and  $f$ , which now represents the acoustic field on an array for times  $t>0$  after it has propagated through the hydrodynamically evolving environments illustrated in Figs. 2 and 10. This correlation then represents a measure of the contribution of internal waves and tides versus what would be expected if the acoustic responses were only due to water depth variations, and will be used to the end of this section. Fig. 12(b) presents a region of rapid variation near the midbreak bearing, the site of the largest advection of the thermocline. The correlation-decorrelation patterns in the break region roughly mimic contours of thermocline displacement for  $t<12$  h. As internal waves propagate seaward, (e.g., those generated at  $t=9$  or 26 h in Fig. 10), the correlation varies rapidly in the bands within the boxes labeled A in Fig. 12(b). The bands sweep past the arrays near the bottom of the break, corresponding to large

loss [cf. arrows in Fig. 11(a)]; this loss is related to acoustic refraction from internal waves. The bands then fade for bearings away from the break as the direction of acoustic propagation for these bearings more closely aligns with the internal wave's propagation vector. During the low tide periods for  $t > 12$  h, the periodic sound speed variation causes correlation to be consistently reduced to about 0.8 on the shelf. In Fig. 12(d), the largest decrease in correlation (arrows labeled B) is associated with downwelling at the deep end of the shelf break. Along the midbreak, ring-like patterns of periodic re-correlation occur at approximately 3, 14, 25, and 28 h, corresponding to the high loss regions seen in Fig. 11(b) where the latter occur during downwelling events. At 8 and 20 h similar elongated patterns occur during downwelling localized over the bottom of the break. In Fig. 12(f), the strongest decorrelation is in deep water at around 14 h and between 25 and 28 h, during high transmission loss periods illustrated in Fig. 11(c). The rapid variation in correlation patterns along the source isobath are less regular than in Fig. 12(d), but remain associated with high loss regions of Fig. 11(c). As in Fig. 12(b), bands of strong, rapid variation of correlation progress with the internal waves' propagation into shallow water, at the boxes labeled C.

#### IV. SUMMARY AND DISCUSSION

Numerical simulations have been presented for acoustic propagation in a canonical shelf-break ocean environment. They included hydrodynamic specification of the space and time varying sound speed field for the purpose of studying some of the effects of sub-mesoscale oceanography on acoustic field structure. The evolution of the environment was determined in a physically consistent manner with respect to tidal forcing and stratified flows so that internal tides and solibores could be simulated from generation through evolution and propagation. The influence of these oceanographic features on acoustic propagation was illustrated with several 2D and 3D acoustic examples.

The simulations produced acoustic fields propagating within an ocean waveguide where tidally induced water depth variations, internal tides and solibores co-existed and were coupled together. Sample computations describing the frequency and time dependence of signal gain degradation on vertical arrays were presented for two 30 minute time windows. During these periods, the water depth changes induced by the barotropic tide were small (less than .5 m), and this change was reflected in the relatively weak dependence between these variations and SGD. The SGD was dominated by phase rather than amplitude contributions throughout the 200–500 Hz frequency band. There were, however, significant amplitude contributions over several frequency subbands for short range (11 km) propagation during a time interval in which a wave packet crosses the array and the local source environment was approximately time independent. For the short period (30 min) cases, weak degradation was generally observed over the first 2–3 min for the 200–500 Hz band, followed by enhanced degradation whose overall strength exhibited strong frequency and source depth dependence as the environment evolved. Occasionally, fre-

quency selective recorelation of the signal up to 10 dB was observed. It is interesting to note that both phase dominance of the SGD and recorelation of the field are consistent with results observed from data and previous modeling efforts<sup>31,33</sup> though no significant effort was made here to model a specific environment. Detection range was estimated for several frequency bands, after performing some spatial averaging of the field intensity. Higher acoustic frequencies were related to decreases in detection range. Smaller decreases in detection range were found when only the tidal variations were present (no internal waves); larger decreases in detection range were obtained when both the tide and internal waves were present, representing the case of fully stratified flow.

Angular (azimuthal) variations in the acoustic field in the vicinity of the shelf break were studied by “extending” the environment in the along-slope direction in conjunction with 3D acoustic computations to propagate the field onto a set of vertical arrays positioned at fixed range and variable azimuth. Depth averaged transmission loss showed several interesting features, including horizontal refraction by the sloping bathymetry and enhanced loss that was time locked to downwelling at the shelf break. Azimuth-time correlation plots were computed for pressure fields on these arrays in order to estimate the relative importance of volume variability and water depth changes, both of which were driven by tidal flow. The sources were placed near or in the break region and the hydrodynamic changes at the break, such as downwelling, dominated the temporal correlation of the acoustic field.

Using the numerical results obtained for the simplified shelf-break environment as a rough guide, one can make some observations concerning sonar performance prediction and phase sensitive signal processors operating in these regions. For example, in shelf-break regions where tidal flow has a significant impact on determining environmental variability, phase-sensitive processors (e.g., matched field or matched mode localization schemes) should adaptively control the frequency band(s) of the replica fields, due to the significant frequency and time dependence of both the degradation and detection range observed here. The acoustic replica vectors would need to be updated in a manner consistent with the rate of signal gain degradation observed in the simulations; for some frequency bands a cyclic update may be appropriate given the observed re-correlation of the field. Because the degradation is a function of M2 tidal phase, the updates should account for this phase-locking behavior. Since the acoustic response in this environment is not shift invariant with respect to space or time, it appears that phase sensitive processors may need to be tuned for each specific environment and source-receiver combination that might be encountered. It should be noted that sonar performance is dependent on other factors not considered here. For example, neither a background (spatially diffuse) internal wave field nor an ambient surface generated noise field were included in this study, though both can negatively impact sonar performance. Other factors that can influence SGD and detection range are acoustic wave scattering from rough bathymetry or bottom inhomogeneity; each can be a contributor to a loss of field coherence. The relative importance

of the surface, volume and bottom contributions is a function of acoustic frequency and is also time and site dependent. While one of these components may dominate under a particular set of environmental conditions, it is often the case that multiple components are found to contribute to the SGD and detection range, and their contributions are not necessarily independent. Additional degrees of freedom due to the introduction of horizontal anisotropy in bathymetry and/or volume variability produces an azimuthal component to the above-mentioned quantities and is reflected in the shift-variant nature of the acoustic field.

Though the ocean model was initiated with a typical summer thermocline profile from the New Jersey shelf, there was no attempt to characterize a specific littoral environment in detail. Although some results are qualitatively consistent with shallow water measurements, considerable care should be exercised in directly relating specific model results to experimental data. This raises the issue of the predictive capability of such models, a subject not directly considered in this paper. Model-data comparisons are impacted by a number of factors. For example, as noted in the Introduction, environmental data are invariably undersampled in space and time; initialization of a numerical (environmental) model typically requires a much finer sampling than can be supplied by the data. The sampling requirements for initialization of submesoscale models are much more difficult to satisfy than those associated with mesoscale models since the latter ignore situations where the ratio of the horizontal to vertical scales in the fluid motion approaches unity. In addition, the finite spatial and temporal scales used in the simulation place limits on acoustic field predictability because they restrict the level of physical description included in the model. For example, this study precluded fine structure and turbulence in the environmental specification because of the relatively coarse grid sampling used in the simulations.

The oceanographic model described here can be fully implemented in three dimensions, though in this paper the flows are restricted to two-dimensional motion. Along-slope variation in the oceanography would introduce additional degrees of freedom (and realism) in the azimuthal dependence of the acoustic field, beyond that illustrated in Sec. III.

Although the above considerations fall outside the scope of this paper, they are points that need to be evaluated in developing a simulation based prediction scheme for sonar performance using vertical or horizontal arrays. Some of the above-mentioned issues can be resolved through modeling enhancements and higher resolution initialization. There exists, however, a deeper issue affecting the general ability of numerical models to make accurate and robust predictions of acoustic field quantities. This issue is related to the question of how one can quantify the lack of knowledge or uncertainty concerning the basic “ingredients” that enter into a numerical simulation. Most numerical modeling studies, including this one, employ inherently deterministic computations of the acoustic field through the solution of a deterministic wave equation. Uncertainty estimates in the boundary conditions, parameters and fields that drive the numerical simulations are not supplied to the algorithm(s). Without such estimates, simulation-based prediction schemes cannot

be objectively assessed. Embedding environmental uncertainty directly into the computations is a non-trivial problem.<sup>36,37</sup> In order to develop a robust numerical prediction capability, however, environmental uncertainty should be quantified and included as an integral part of a simulation-based prediction system.

## ACKNOWLEDGMENTS

The authors wish to thank both the Office of Naval Research for support through NRL Base Funding, and the anonymous reviewers for a number of constructive comments on the manuscript.

- <sup>1</sup>J. R. Apel, M. Badiey, C. S. Chiu, S. Finette, R. Headrick, J. Kemp, J. F. Lynch, A. Newhall, M. H. Orr, B. H. Pasewark, D. Tielburger, A. Turgut, K. von der Heydt, and S. Wolf, “An overview of the 1995 SWARM shallow-water internal wave acoustic scattering experiment,” *IEEE J. Ocean. Eng.* **22**, 465–500 (1997).
- <sup>2</sup>D. Tielburger, S. Finette, and S. Wolf, “Acoustic propagation through an internal wave field in a shallow water waveguide,” *J. Acoust. Soc. Am.* **101**, 787–808 (1997).
- <sup>3</sup>J. Preiseg and T. F. Duda, “Coupled acoustic mode propagation through continental-shelf internal solitary waves,” *IEEE J. Ocean. Eng.* **22**, 256–269 (1997).
- <sup>4</sup>B. G. Katsnel’son and S. A. Pereselkov, “Resonance effects in sound scattering by internal wave packets in a shallow sea,” *Acoust. Phys.* **44**, 786–792 (1998).
- <sup>5</sup>S. Finette, M. H. Orr, A. Turgut, J. Apel, M. Badiey, C. S. Chiu, R. H. Headrick, J. N. Kemp, J. F. Lynch, A. E. Newhall, K. von der Heydt, B. Pasewark, S. N. Wolf, and D. Tielburger, “Acoustic field variability induced by time-evolving internal wave fields,” *J. Acoust. Soc. Am.* **108**, 957–972 (2000).
- <sup>6</sup>D. Rubenstein, “Observations of cnoidal internal waves and their effect on acoustic propagation in shallow water,” *IEEE J. Ocean. Eng.* **24**, 346–357 (1999).
- <sup>7</sup>M. Badiey, Y. Mu, J. Lynch, J. Apel, and S. Wolf, “Temporal and azimuthal dependence of sound propagation in shallow water with internal waves,” *IEEE J. Ocean. Eng.* **27**, 117–129 (2002).
- <sup>8</sup>B. G. Katsnel’son and S. A. Pereselkov, “Low-frequency horizontal acoustic refraction caused by internal wave solitons in a shallow sea,” *Acoust. Phys.* **46**, 684–691 (2000).
- <sup>9</sup>M. Badiey, B. G. Katsnel’son, J. F. Lynch, S. Pereselkov, and W. L. Siegmann, “Measurement and modeling of three-dimensional sound intensity variations due to shallow-water internal waves,” *J. Acoust. Soc. Am.* **117**, 613–625 (2005).
- <sup>10</sup>S. Finette and R. Oba, “Acoustic field variability induced by internal solitary waves on a continental shelf,” in *Proceedings of the Institute of Acoustics*, edited by T. G. Leighton, G. J. Heald, H. D. Griffiths, and G. Griffiths (Bath University Press, Bath, UK, 2001), Vol. **23**, pp. 321–326.
- <sup>11</sup>R. Oba and S. Finette, “Acoustic propagation through anisotropic internal wave fields: Transmission loss, cross-range coherence, and horizontal refraction,” *J. Acoust. Soc. Am.* **111**, 769–784 (2002).
- <sup>12</sup>S. Finette and R. Oba, “Horizontal array beamforming in an azimuthally anisotropic internal wave field,” *J. Acoust. Soc. Am.* **114**, 131–144 (2003).
- <sup>13</sup>*Oceanography and Acoustics: Prediction and Propagation Models*, edited by A. R. Robinson and D. Lee (AIP Press, New York, 1994).
- <sup>14</sup>R. C. Rhodes, H. E. Hurlburt, A. J. Wallcraft, C. N. Barron, P. J. Martin, E. J. Metzger, J. F. Shriver, D. S. Ko, O. Smedstad, S. L. Cross, and A. Kara, “Navy real-time global modeling systems,” *Oceanogr.* **15**, 29–43 (2002).
- <sup>15</sup>K. Lamb, “Numerical experiments of internal wave generation by strong tidal flow across a finite amplitude bank edge,” *J. Geophys. Res.*, [Oceans] **99**(1), 843–864 (1994).
- <sup>16</sup>K. Winters, “Simulation of non-hydrostatic, density-stratified flow in irregular domains,” *Int. J. Numer. Methods Fluids* **32**, 263–284 (2000).
- <sup>17</sup>C. Shen, “Constituent boussinesq equations for waves and currents,” *J. Phys. Oceanogr.* **31**, 850–859 (2001).
- <sup>18</sup>C. Y. Shen and T. E. Evans, “A free-surface hydrodynamic model for density-stratified flow in the weakly to strongly nonhydrostatic regime,” *J. Comput. Phys.* **200**, 695–717 (2004).

- <sup>19</sup>P. C. Gallacher, S. Piacek, and D. Dietrich, in *Estuarine and Coastal Modeling*, Proceedings of the 7th International Conference of American Society of Civil Engineers, 2001, pp. 204–214.
- <sup>20</sup>S. Finette, R. Oba, P. Gallacher, and M. Schafferkotter, “Acoustic field propagation through a time-evolving buoyant jet,” *J. Acoust. Soc. Am.* **115**, 2550 (2004).
- <sup>21</sup>S. Finette, T. Evans, and C. Shen, “Submesoscale modeling of environmental variability in a shelf-slope region and the effect on acoustic fluctuations” in *Impact of Littoral Environmental Variability on Acoustic Predictions and Sonar Performance*, edited by N. G. Pace and F. B. Jensen (Kluwer Academic, Boston, 2002), pp. 401–408.
- <sup>22</sup>S. A. Chin-Bing, A. Warn-Varnas, D. B. King, K. G. Lamb, M. Teixeira, and J. A. Hawkins, “Analysis of coupled oceanographic and acoustic soliton simulations in the Yellow Sea: a search for soliton-induced resonances,” *Math. Comput. Simul.* **62**, 11–20 (2003).
- <sup>23</sup>P. K. Kundu, *Fluid Mechanics* (Academic, New York, 1990).
- <sup>24</sup>F. J. Millero and A. Poisson, “International one-atmosphere equation of state of seawater,” *Deep-Sea Res., Part A* **28A**, 625–629 (1981).
- <sup>25</sup>V. A. Del Grosso, “New equation for the speed of sound in natural waters (with comparisons to other equations),” *J. Acoust. Soc. Am.* **56**, 625–629 (1981).
- <sup>26</sup>M. D. Collins, “A split-step Padé solution for the parabolic equation method,” *J. Acoust. Soc. Am.* **93**, 1736–1742 (1993).
- <sup>27</sup>D. Lee and M. H. Schultz, *Numerical Ocean Acoustic Propagation in Three Dimensions* (World Scientific, Singapore, 1995).
- <sup>28</sup>A. P. Rosenberg, “A new rough surface parabolic equation program for computing low-frequency acoustic forward scattering from the ocean surface,” *J. Acoust. Soc. Am.* **105**, 144–153 (1999).
- <sup>29</sup>M. H. Orr and P. C. Mignerey, “Matched-field processing gain degradation caused by tidal flow over continental shelf bathymetry,” *J. Acoust. Soc. Am.* **111**, 2615–2620 (2002).
- <sup>30</sup>R. H. Headrick, J. F. Lynch, J. N. Kemp, A. E. Newhall, K. von der Heydt, J. Apel, M. Badiéy, C. S. Chiu, S. Finette, M. Orr, B. Pasewark, A. Turgut, S. Wolf, and D. Tielbuerger, “Acoustic normal mode fluctuation statistics in the 1995 SWARM internal wave scattering experiment,” *J. Acoust. Soc. Am.* **107**, 201–220 (2000).
- <sup>31</sup>P. C. Mignerey and M. H. Orr, “Observations of matched-field autocorrelation time in the South China Sea” *IEEE J. Ocean. Eng.* **29**, 1280–1291 (2004).
- <sup>32</sup>C. S. Chiu, “Realistic simulation studies of acoustic signal coherence in the presence of an internal soliton wavepacket,” in *The 1998 WHOI/IOS/ONR Internal Solitary Wave Workshop: Contributed Papers*, WHOI Tech Report WHOJ-99-07, 1999.
- <sup>33</sup>D. Rouseff, A. Turgut, S. N. Wolf, S. Finette, M. H. Orr, B. H. Pasewark, J. R. Apel, M. Badiéy, C. Chiu, R. H. Headrick, J. F. Lynch, J. N. Kemp, A. E. Newhall, K. von der Heydt, and D. Tielbuerger, “Coherence of acoustic modes propagating through shallow water internal waves,” *J. Acoust. Soc. Am.* **111**, 1655–1666 (2002).
- <sup>34</sup>D. R. DelBalzo, C. Feuillade, and M. M. Rowe, “Effects of water-depth mismatch on matched-field localization in shallow water,” *J. Acoust. Soc. Am.* **83**, 2180–2185 (1988).
- <sup>35</sup>A. Tolstoy, S. Jesus, and O. Rodriguez, “Tidal effects on mfp via the INTIMATE96 test,” in *Impact of Littoral Environmental Variability on Acoustic Predictions and Sonar Performance*, edited by N. G. Pace and F. B. Jensen (Kluwer Academic, Boston, 2002), pp. 457–463.
- <sup>36</sup>S. Finette, “Embedding uncertainty into ocean acoustic propagation models,” *J. Acoust. Soc. Am.* **117**, 997–1000 (2005).
- <sup>37</sup>S. Finette, “A stochastic representation of environmental uncertainty and its coupling to acoustic wave propagation in ocean waveguides,” *J. Acoust. Soc. Am.* **120**, 2567–2579 (2006).